npj | quantum materials

Article

Published in partnership with Nanjing University

https://doi.org/10.1038/s41535-024-00711-w

Topological phase transition in quasi-one-dimensional bismuth iodide Bi_4I_4

W. X. Zhao[1], M. Yang[2,3], X. Du[1], Y. D. Li[1], K. Y. Zhai[1], Y. Q. Hu[1], J. F. Han[4,5], Y. Huang[4,5], Z. K. Liu[6,7], Y. G. Yao[4,5], J. C. Zhuang[2,3], Y. Du[2,3] ✉, J. J. Zhou[4] ✉, Y. L. Chen[6,7,8] ✉ & L. X. Yang[1,9,10] ✉

Quasi-one-dimensional (quasi-1D) bismuth iodide Bi_4I_4 exhibits versatile topological phases of matter including weak topological insulator (WTI) and higher-order topological insulator (HOTI) phases with high tunability in response to external parameters. In this work, performing laser-based angle-resolved photoemission spectroscopy with submicron spatial resolution (micro-ARPES), we reveal the presence of an energy gap on the (100) surface of the low-temperature α-Bi_4I_4, providing spectroscopic evidence for the HOTI phase. Conversely, the high-temperature β-Bi_4I_4 harbors gapless Dirac fermions on the (100) surface alongside gapped states on the (001) surface, thereby establishing a WTI phase. By tracking the temperature evolution of the (100) surface states, we unveil a thermal hysteresis of the surface gap in line with the α-β structural phase transition. Our findings directly evidence a temperature-induced topological phase transition from WTI to HOTI in Bi_4I_4, which paves the way to its potential applications at room temperature.

Topological quantum phase transitions (TQPTs) represent a fascinating type of phase transitions characterized by global topological invariants, which diverge from the conventional symmetry-breaking phase transitions described by local order parameters. TQPTs not only hold significant scientific implications for elucidating topological properties under external perturbations[1–5] but also pave an avenue for the utilization of topological quantum materials with high tunability in future electronic and spintronic devices[6–9]. Throughout a TQPT, the ground-state wavefunction evolves with a controlling parameter such as strain, chemical substitution, electric field, and temperature[10–17], typically associated with a change in the energy gap of the boundary states.

Recently, quasi-one-dimensional (quasi-1D) bismuth halides Bi_4X_4 (X = Br, I) have garnered great research attention owing to the abundant topological quantum phases in this family compounds, including strong/weak topological insulator[18–20], higher-order topological insulator[21–23], and Weyl semimetal[24]. These intriguing topological quantum phases are sensitive to the stacking sequence and interlayer coupling of Bi_4X_4 layers constituting the bulk crystals[25–27]. By manipulating external conditions, e.g., tuning temperature, applying strain or chemical substitution, TQPT can be established and feasibly controlled.

Taking Bi_4I_4 as an example, monolayer Bi_4I_4 consists of arrays of chains along the b axis, which has been verified as near a 2D quantum spin Hall (QSH) insulator/normal insulator phase boundary[28–30]. Bulk α/β-Bi_4I_4 share the same chain structure except that the α-phase comprises two Bi_4I_4 chains relatively shifting along the a axis in a unit cell (Fig. 1a, b). Consequently, the interaction between the QSH edge states in each Bi_4I_4 monolayer is distinctive in the two phases. For β-Bi_4I_4, the monolayers stack along c with the metallicity of the side surface preserved by the symmetry, realizing a WTI phase[4,12,31–34]. By contrast, the adjacent QSH edge states are in different chemical environments in α-Bi_4I_4. Therefore, the hybridization between adjacent QSH edge states induces gapped (100) surface states (Fig. 1b, c). Remarkably, for particular stacking sequences, gapless modes, namely topological hinge states, survive at the hinges of the crystal as enforced by the higher-order bulk-boundary correspondence (see the red dots in Fig. 1b)[27,35]. Since the dimensional difference between the bulk and conducting boundary mode is larger than 1, this intriguing topological state is classified as a

[1]State Key Laboratory of Low Dimensional Quantum Physics, Department of Physics, Tsinghua University, Beijing, China. [2]School of Physics, Beihang University, Beijing, China. [3]Centre of Quantum and Matter Sciences, International Research Institute for Multidisciplinary Science, Beihang University, Beijing, China. [4]Centre for Quantum Physics, Key Laboratory of Advanced Optoelectronic Quantum Architecture and Measurement (MOE), School of Physics, Beijing Institute of Technology, Beijing, China. [5]International Center for Quantum Materials, Beijing Institute of Technology, Zhuhai, China. [6]School of Physical Science and Technology, ShanghaiTech University and CAS-Shanghai Science Research Center, Shanghai, China. [7]ShanghaiTech Laboratory for Topological Physics, Shanghai, China. [8]Department of Physics, Clarendon Laboratory, University of Oxford, Oxford, UK. [9]Frontier Science Center for Quantum Information, Beijing, China. [10]Collaborative Innovation Center of Quantum Matter, Beijing, China. ✉e-mail: yi_du@buaa.edu.cn; jjzhou@bit.edu.cn; yulin.chen@physics.ox.ac.uk; lxyang@tsinghua.edu.cn

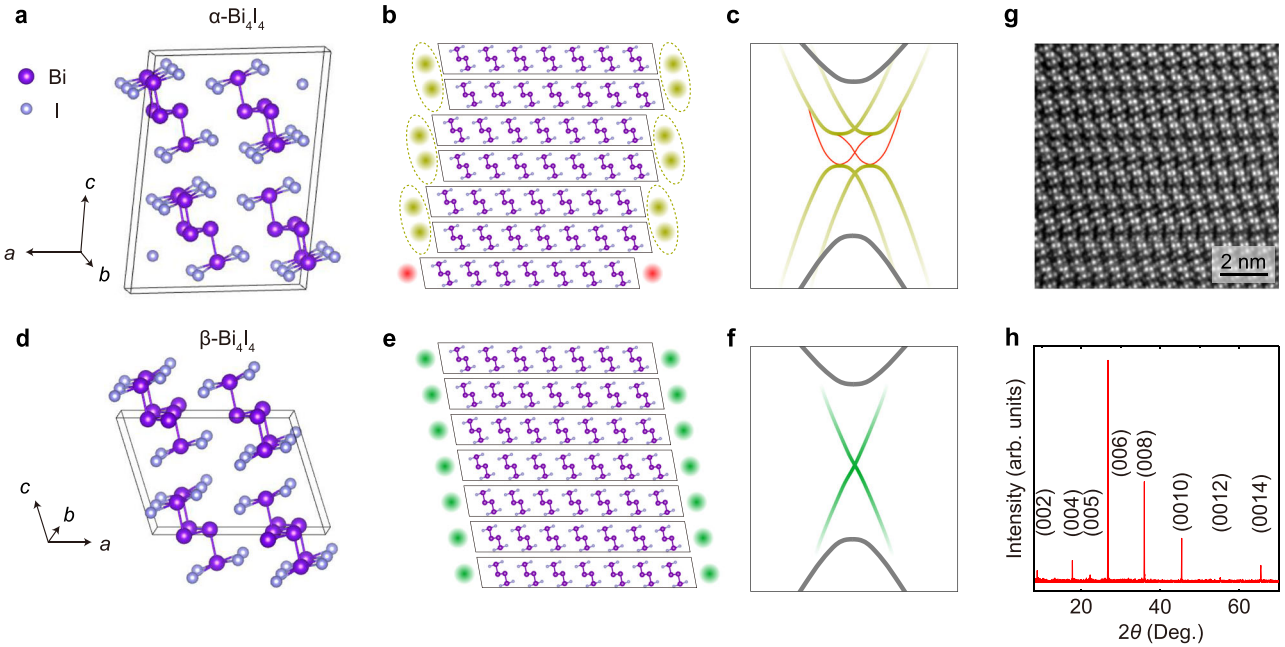

Fig. 1 | Topological properties and crystal structures of α/β-Bi_4I_4. **a** The crystal structure of α-Bi_4I_4. The black lines indicate the unit cell. **b** Schematic illustration of the boundary states on the (100) surfaces. Each dot represents the QSH edge state of a Bi_4I_4 monolayer. The yellow-dot pair in an ellipse and red dots represent the quantum-hybridized (100) surface states and the topological hinge states, respectively. **c** Illustration of the electronic structure of α-Bi_4I_4 on the (100) side surface. The gray, yellow, and red curves indicate the bulk, surface, and hinge states, respectively. **d**–**f** The same as (**a**–**c**) except for β-Bi_4I_4. The green dots in (**e**) and green curves in (**f**) represent the topological surface states on the (100) surface of β-Bi_4I_4. **g** Cross-section image of the (010) surface of α-Bi_4I_4 with atomic resolution measured with scanning transmission electron microscope (STEM). **h** X-ray diffraction measurements of α-Bi_4I_4. The STEM and XRD measurements are performed at 298 K.

HOTI. Upon increasing temperature, α-Bi_4I_4 undergoes a structural transition to β-Bi_4I_4[36], establishing a temperature-induced TQPT.

Angle-resolved photoemission spectroscopy (ARPES), serving as a powerful tool to elucidate the electronic structure of single crystals, has been performed to unravel the band structure of bismuth halides[26,37–40]. While high-resolution laser-ARPES experiments have shown evidence for the HOTI phase in α-Bi_4Br_4, the investigation of Bi_4I_4 is more intricate[35,41,42]. Gapless (100) surface states have been observed in β-Bi_4I_4[35,41], confirming its non-trivial topological property. However, there are still debates on the existence of gapless surface states on the (001) surface, making it elusive whether β-Bi_4I_4 is a WTI or strong topological insulator (STI). As for α-Bi_4I_4, although a gapped (100) surface state has been detected at the $\bar{\Gamma}_{100}$ point[35] in accordance with the theoretical prediction, further confirmation is still required to ascertain whether the side surface states are fully gapped over the whole surface Brillouin zone (especially at the $\bar{Z}$ point) and conclusively identify the HOTI phase. Moreover, only a subtle change of the width of ARPES spectra was observed across the structural transition[35], with the temperature-evolution of the fine electronic structure, especially the surface gap, yet to be investigated.

In this work, by performing laser-based micro-ARPES measurements with high energy and momentum resolution[37,43], we systematically investigate the temperature evolution of the electronic structure of Bi_4I_4. At low temperatures, we observe gaps of about 40 meV and 5 meV at the $\bar{\Gamma}_{100}$ and $\bar{Z}$ points on the (100) surface, confirming the HOTI phase of α-Bi_4I_4 (Fig. 2c). With increasing temperature, we directly observe the evolution of the gapped surface states into a gapless Dirac fermion across the transition temperature T_S~300 K. The magnitude of the gap shows a thermal hysteretic behavior, confirming the first-order nature of the TQPT. Moreover, our measurements unveil that a fully gapped (001) surface of β-Bi_4I_4, which, together with the gapless topological surface states (TSSs) on the (100) surface, compellingly evidences the WTI phase of β-Bi_4I_4 (Fig. 2d). Our experimental observations are in excellent agreement with ab-initio calculations and provide more systematic insights into the TQPT of quasi-1D Bi_4I_4.

Results

Electronic structure and topological property of α-Bi_4I_4

Figure 3a shows the ARPES spectrum of α-Bi_4I_4 at the $\bar{\Gamma}_{100}$ point on the (100) surface. We resolve valence and conduction bands of the (100) surface states, characterizing the splitting feature and surface gap caused by hybridization of the QSH edge states from adjacent Bi_4I_4 layers (Fig. 1c). According to the curvature spectra in Fig. 3c, the energy gap between the valence and conduction band is estimated to be about 31 meV (the peak-to-peak gap between the band crossing points at $\bar{\Gamma}_{100}$ is about 40 meV). At the $\bar{Z}$ point, the surface states exhibit a Dirac-cone-like dispersion with a gap of about 7 meV (Fig. 3b, d). Our measurements agree with the calculation in Fig. 3e, f. The gapped dispersion at $\bar{Z}$ can be further evidenced by fitting the Dirac dispersion as shown in Fig. 3b. The band dispersion is firstly extracted by fitting the momentum distribution curves (MDCs) to the Lorentzians (represented by the green dots). Then the upper and lower branches of the extracted dispersion are fitted to linear dispersions. The energy interval between the crossing points of the upper and lower branches indicates an energy gap of about 5 meV at the Dirac point, in line with the curvature analysis (Fig. 3d) and the theoretical calculation (Fig. 3f).

Figure 3g, h shows the laser-ARPES spectra of α-Bi_4I_4 measured on the (001) surface with their curvature plots shown in Figs. 3i and 3j, respectively. Around the $\bar{\Gamma}_{001}$ point, we observe a band gap over 395 meV without the conduction band observed. At the $\bar{M}$ point, we observe a direct band gap of about 170 meV. Both the experiments at $\bar{\Gamma}_{001}$ and $\bar{M}$ are well reproduced by the theoretical calculation of the bulk states, suggesting the absence of topological surface states on the (001) surface of α-Bi_4I_4. Therefore, our results on the (001) and (100) surfaces confirm the HOTI phase of α-Bi_4I_4, resembling the results of α-Bi_4Br_4[37]. We do not resolve explicit signals from

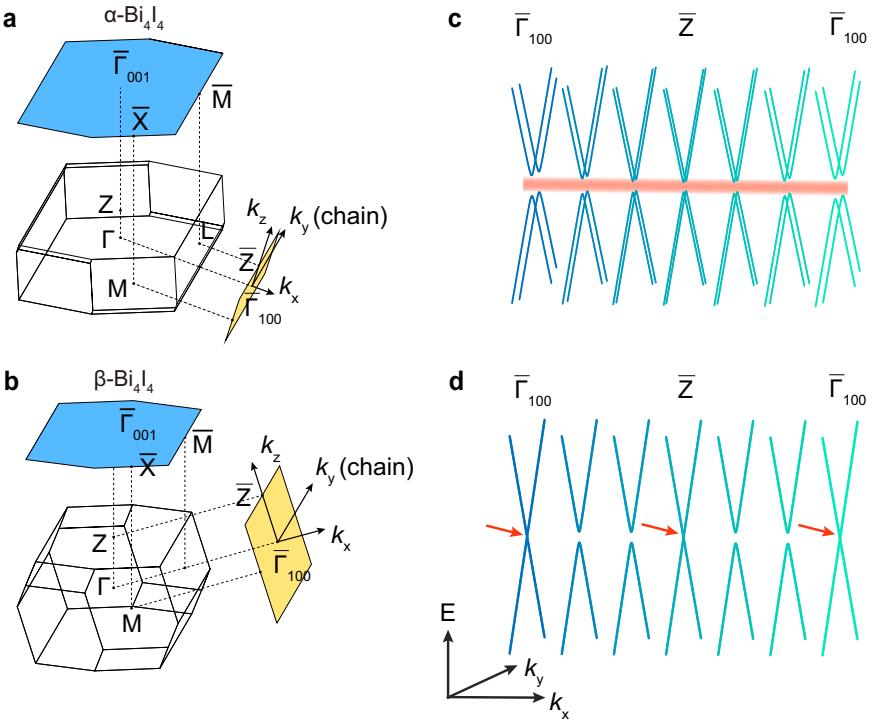

Fig. 2 | Brillion zone and boundary electronic structures of α/β-Bi_4I_4. **a**, **b** Bulk and surface Brillouin zones of α/β-Bi_4I_4 with high-symmetry points indicated, respectively. **c**, **d** Schematics showing the surface band structure of HOTI phase of α-Bi_4I_4 and WTI phase of β-Bi_4I_4. The blue curves and the red line indicate the (100) surface states and in-gap hinge states, respectively. The red arrows indicate the location of the gapless Dirac fermions.

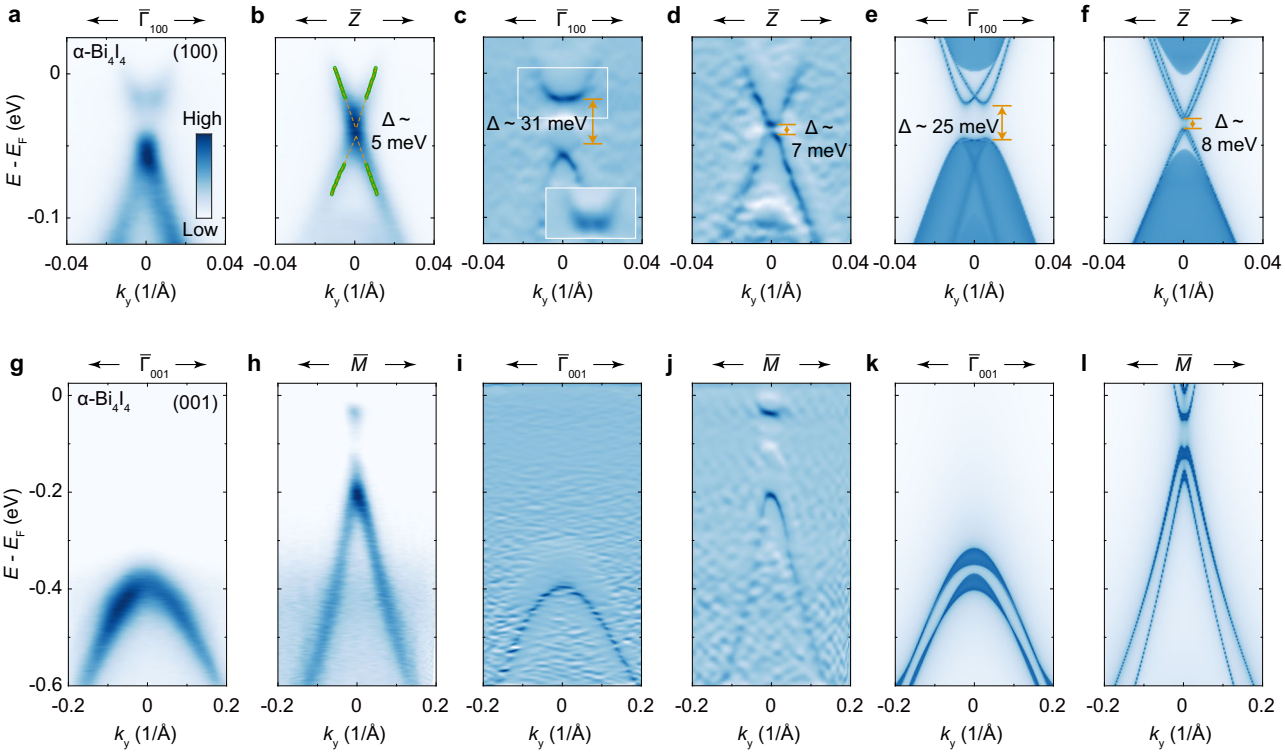

Fig. 3 | Fine electronic structure of α-Bi_4I_4 on the (100) and (001) surfaces. **a**, **b** Band structure of the (100) surface states at the $\bar{\Gamma}_{100}$ and $\bar{Z}$ points measured by laser-based micro-ARPES. The green dots in (**b**) are determined by fitting the momentum distribution curves (MDCs) to Lorentzians and the yellow dashed lines are the fit of the extracted dispersion to the massive Dirac-fermion dispersion. **c**, **d** Curvature plots of the ARPES spectra in (**a**) and (**b**). **e**, **f** (100) surface-projected band structures calculated at the $\bar{\Gamma}_{100}$ and $\bar{Z}$ points, respectively. **g**, **h** ARPES spectra of α-Bi_4I_4 at the $\bar{\Gamma}_{001}$ and $\bar{M}$ points on the (001) surface. **i**, **j** Curvature plots of the ARPES spectra in (**g**) and (**h**). (**k**, **l**) (001) surface-projected band structures calculated at the $\bar{\Gamma}_{001}$ and $\bar{M}$ point, respectively. Data were measured along the chain direction at 80 K using LH-polarized 7-eV laser.

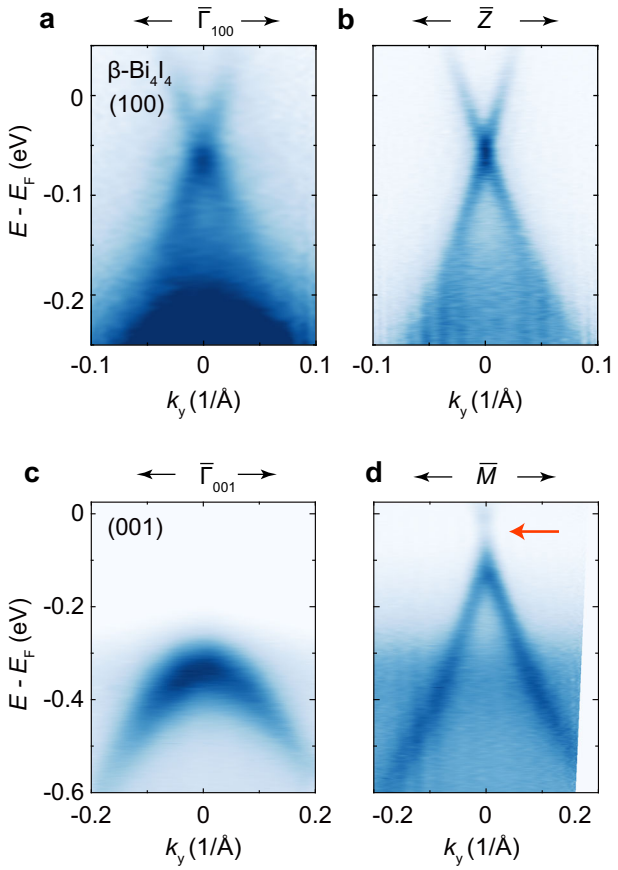

Fig. 4 | Electronic structure of β-Bi_4I_4 on the (100) and (001) surface. a, **b** ARPES spectra of β-Bi_4I_4 at $\bar{\Gamma}_{100}$ and $\bar{Z}$ point on the (100) surface, respectively. **c**, **d** ARPES spectra of β-Bi_4I_4 at $\bar{\Gamma}_{001}$ and $\bar{M}$ point on the (001) surface, respectively. The red arrow indicates the energy gap at the $\bar{M}$ point. The spectra were measured along the chain direction at 316 K using LH-polarized 7-eV laser.

the topological hinge states, possibly due to the weak photoemission intensity from the hinge states and relatively small (100) surface gap of α-Bi_4I_4.

Electronic structure and topological property of β-Bi_4I_4

Next, we examine the electronic structure of the (100) surface of β-Bi_4I_4 at 316 K. As shown in Fig. 4a, b, β-Bi_4I_4 shows a gapless Dirac fermion dispersion at both $\bar{\Gamma}_{100}$ and $\bar{Z}$ point. As to (001) surface, β-Bi_4I_4 exhibits a band gap of 330 meV (between the valence band top and E_F) and 125 meV (between the valence band top and the conduction band bottom) at the $\bar{\Gamma}_{001}$ and $\bar{M}$ points, respectively, similar to α-Bi_4I_4 (Fig. 4c, d). Compared to α-Bi_4I_4, the valence and conduction band of β-Bi_4I_4 shift up slightly with a weak residual spectral weight of the conduction band at E_F. We do not observe any signature of topological surface states on the (001) surface, which is in line with the WTI phase of β-Bi_4I_4.

Topological phase transition of Bi_4I_4

In order to study the topological phase transition of bismuth iodide, we perform systematic ARPES measurements at different temperatures across T_S. At 80 K, the data at the $\bar{\Gamma}_{100}$ point (Fig. 5a) clearly shows a gap, consistent with the (100) surface states of α-Bi_4I_4 in Fig. 3a. With increasing temperature up to around 310 K, the energy interval between the surface valence and conduction band at the $\bar{\Gamma}_{100}$ point slightly decreases. The spectra also get blurred at high temperatures, which may indicate a preclude of crystal transformation related to the structural transition instead of thermal broadening effect[35]. Prominently, above T_S, the surface gap is suddenly suppressed and the dispersion shows a single gapless Dirac dispersion (Fig. 5g), which confirms the WTI phase of β-Bi_4I_4 together with the gapped spectra on the (001) surface (Fig. 4). Simultaneously, the spectrum becomes much sharper with the full width at the half maximum changed from about 0.01 $Å^{-1}$ (302 K) to 0.007 $Å^{-1}$ (316 K). This band sharpening of surface states is because of the bilayer splitting of α-Bi_4I_4 (Fig. 1c) and has been revealed by the previous experiments[35]. As the temperature decreases, the spectrum recovers at low temperatures and the surface gap reemerges (Fig. 5h–k).

The temperature evolution of the (100) surface gap extracted by double-Lorentzian fitting the EDC at $\bar{\Gamma}_{100}$ is summarized in Fig. 5l, which exhibits a thermal hysteresis loop near the structural transition. Specifically, an α-phase characterization is maintained up to about 310 K in the heating process, which can be confirmed by features such as surface gap and band sharpness mentioned above (Fig. 5a–f). While in the cooling process, a β-phase spectrum with a sharp single Dirac cone is evident even at 295 K in Fig. 5i, in significant contrast to Fig. 5e detected at the same temperature. The hysteresis in the (100) surface gap indicates that Bi_4I_4 undergoes a first-order structural phase transition accompanied by the topological phase transition from a HOTI to a WTI, in accordance with our ab-initio calculation.

Discussion

For a long time, 2D QSH insulators, hosting symmetry-protected 1D edge states immune to backscattering, are expected to promote the development of dissipationless electronics and spintronics devices[4,5,44]. However, the complicated fabrication of 2D-material devices limits the exploration and application of the 1D edge states. By contrast, 1D topological quantum materials such as Bi_4X_4 can be relatively easily synthesized and naturally harbor highly directional topological boundary states with spin-momentum locking property, which are beneficial for the preservation of coherent quantum states. The quasi-1D nature of Bi_4X_4 further allows for the integration into nanowire configurations that are natural and ideal for device engineering. In particular, the novel HOTI phase with hinge states is promising for dissipationless transport, efficient charge-to-spin conversion, topological quantum computation based on the Majorana zero modes, and the realization of spin-triplet superconductivity[45–53]. Furthermore, the TQPT between HOTI and WTI phases in Bi_4I_4 bridged by a first-order structural transition provides a unique opportunity for the controllable manipulation of the topological boundary states near room temperature.

To conclude, we systematically investigate the electronic structure and its temperature evolution of Bi_4I_4. We observe a fully gapped (100) surface state of α-Bi_4I_4, supporting the identification of its HOTI phase. Our measurements at high temperatures confirm the WTI phase of β-Bi_4I_4 by detecting its gapped (001) band structure and gapless (100) TSS. More importantly, we detect the thermal hysteresis loop of the gap in the (100) surface states. Our study unravels the fine band structure of Bi_4I_4 with unprecedented precision and provides solid evidence on the TQPT between HOTI and WTI phases bridged by the structural transition. Our results provide deeper scientific insight and pave the way to promising applications on the novel topological quantum properties of quasi-1D Bi_4I_4.

Methods

Single crystal synthesis and characterization

High-quality Bi_4I_4 single crystals were synthesized using a solid-state reaction and chemical vapor transport method[54]. Figure 1g presents the cross-section image by atomic-resolved scanning transmission electron microscope, which confirms the crystal structure and the high quality of our samples.

Laser-based μ-ARPES measurements

Laser-based μ-ARPES measurements with a sub-micron spatial resolution were conducted at Tsinghua University with the 7-eV laser generated by a $KBe_2BO_3F_2$ (KBBF) crystal and focused by an optics lens[43]. The samples were cleaved in-situ under UHV better than 1×10^{-10} mbar and the data

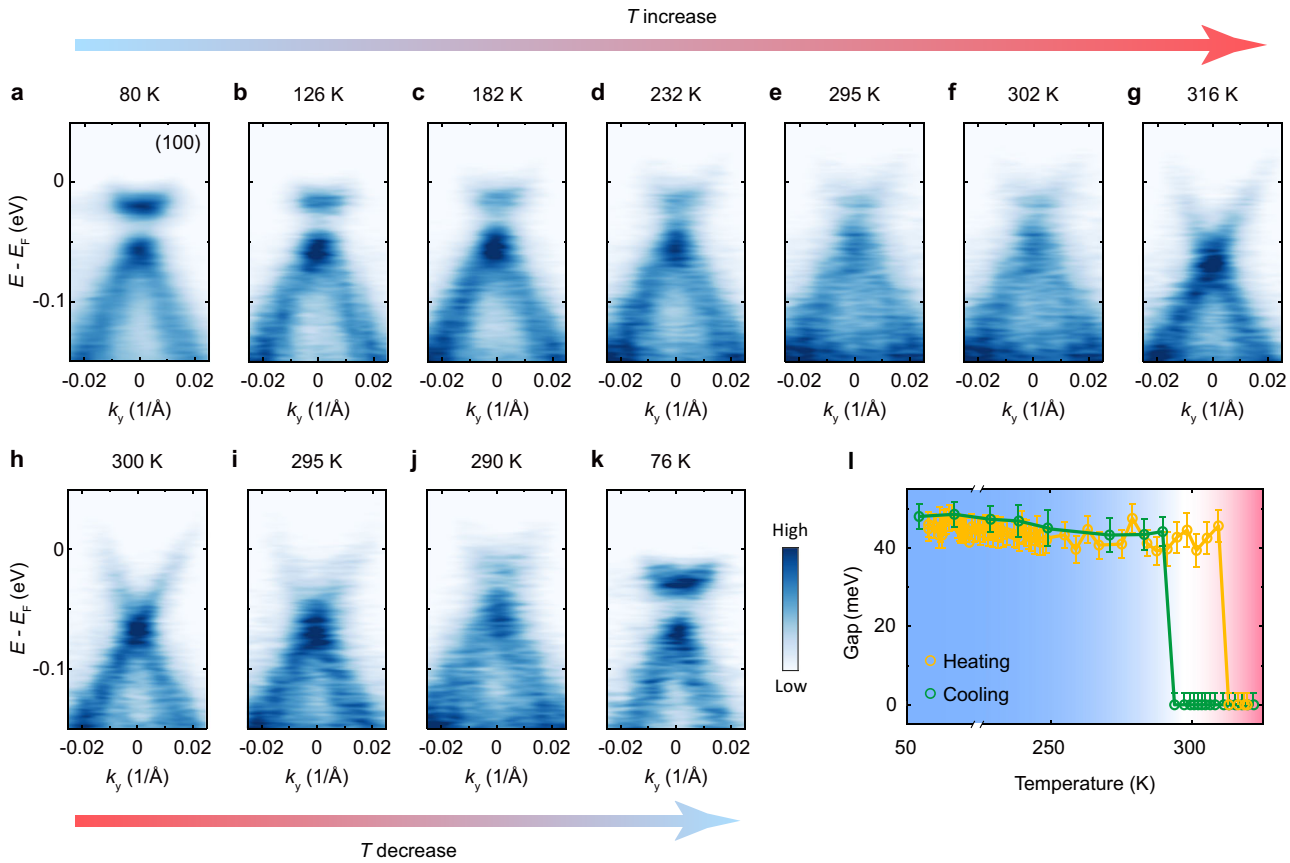

Fig. 5 | Temperature evolution of the (100) surface states across the structural transition. a–k ARPES spectra of the (100) surface states at the $\bar{\Gamma}_{100}$ point of α-Bi_4I_4 (**a**–**g**) and $\bar{Z}$ point of β-Bi_4I_4 (**h**–**k**). The thick arrows indicate the heating or cooling process. Please note the $\bar{\Gamma}_{100}$ point of α-Bi_4I_4 and the $\bar{Z}$ point of β-Bi_4I_4 correspond to almost the same photoelectron emission angle. **l** Temperature evolution of the (100) surface gap showing a hysteresis loop.

were collected by Scienta DA30L electron analyzer. The total energy and angular resolutions were set to 3 meV and 0.2°, respectively.

Ab-initio calculations

First-principles calculations were conducted to investigate the electronic properties and topological band characteristics of bulk Bi_4I_4 using the Vienna ab-initio simulation package[55]. The Heyd-Scuseria-Ernzerhof hybrid functional (HSE06) was employed to describe the exchange-correlation potential[56]. Experimental lattice parameters were used, with the energy cutoff for the plane-wave basis set to 300 eV. Maximally localized Wannier functions (MLWFs) for the p-orbitals of Bi and I atoms were constructed using the WANNIER90 code on a $6 \times 6 \times 3$ k-point mesh[57]. These MLWFs were subsequently applied to build ab initio tight-binding models. Surface electronic structures were calculated by combining the ab-initio tight-binding models with the surface Green function method using our in-house code[58].

Data availability

The data sets that support the findings of this study are available from the corresponding author upon request.

Received: 15 July 2024; Accepted: 19 November 2024;
Published online: 20 December 2024

References

1. Zhang, K. L., Wu, H. C., Jin, L. & Song, Z. Topological phase transition independent of system non-Hermiticity. *Phys. Rev. B* **100**, 045141 (2019).
2. Hasan, M. Z. & Kane, C. L. Colloquium: topological insulators. *Rev. Mod. Phys.* **82**, 3045–3067 (2010).
3. Fu, L. & Kane, C. L. Topological insulators with inversion symmetry. *Phys. Rev. B* **76**, 045302 (2007).
4. Bansil, A., Lin, H. & Das, T. Colloquium: topological band theory. *Rev. Mod. Phys.* **88**, 021004 (2016).
5. Chiu, C.-K., Teo, J. C. Y., Schnyder, A. P. & Ryu, S. Classification of topological quantum matter with symmetries. *Rev. Mod. Phys.* **88**, 035005 (2016).
6. Wuttig, M. & Yamada, N. Phase-change materials for rewriteable data storage. *Nat. Mater.* **6**, 824–832 (2007).
7. Hasan, M. Z. et al. Weyl, Dirac and high-fold chiral fermions in topological quantum matter. *Nat. Rev. Mater.* **6**, 784–803 (2021).
8. Chen, Y. et al. Recent advances in topological quantum materials by angle-resolved photoemission spectroscopy. *Matter* **3**, 1114–1141 (2020).
9. Wieder, B. J. et al. Topological materials discovery from crystal symmetry. *Nat. Rev. Mater.* **7**, 196–216 (2022).
10. Hsieh, D. et al. A topological Dirac insulator in a quantum spin Hall phase. *Nature* **452**, 970–974 (2008).
11. Mutch, J. et al. Evidence for a strain-tuned topological phase transition in $ZrTe_5$. *Sci. Adv.* **5**, eaav9771 (2019).
12. Bernevig, B. A., Hughes, T. L. & Zhang, S.-C. Quantum spin Hall effect and topological phase transition in HgTe quantum wells. *Science* **314**, 1757–1761 (2006).
13. Xu, S.-Y. et al. Topological phase transition and texture inversion in a tunable topological insulator. *Science* **332**, 560–564 (2011).
14. Dziawa, P. et al. Topological crystalline insulator states in $Pb_{1-x}Sn_xSe$. *Nat. Mater.* **11**, 1023–1027 (2012).

15. Xu, S.-Y. et al. Observation of a topological crystalline insulator phase and topological phase transition in $Pb_{1-x}Sn_xTe$. *Nat. Commun.* **3**, 1192 (2012).
16. Wu, L. et al. A sudden collapse in the transport lifetime across the topological phase transition in $(Bi_{1-x}In_x)_2Se_3$. *Nat. Phys.* **9**, 410–414 (2013).
17. Mandal, P. S. et al. Topological quantum phase transition from mirror to time reversal symmetry protected topological insulator. *Nat. Commun.* **8**, 968 (2017).
18. Imura, K.-I., Takane, Y. & Tanaka, A. Weak topological insulator with protected gapless helical states. *Phys. Rev. B* **84**, 035443 (2011).
19. Mong, R. S. K., Bardarson, J. H. & Moore, J. E. Quantum transport and two-parameter scaling at the surface of a weak topological insulator. *Phys. Rev. Lett.* **108**, 076804 (2012).
20. Ringel, Z., Kraus, Y. E. & Stern, A. Strong side of weak topological insulators. *Phys. Rev. B* **86**, 045102 (2012).
21. Tang, F., Po, H. C., Vishwanath, A. & Wan, X. Comprehensive search for topological materials using symmetry indicators. *Nature* **566**, 486–489 (2019).
22. Vergniory, M. G. et al. A complete catalogue of high-quality topological materials. *Nature* **566**, 480–485 (2019).
23. Zhang, T. et al. Catalogue of topological electronic materials. *Nature* **566**, 475–479 (2019).
24. Liu, C.-C., Zhou, J.-J., Yao, Y. & Zhang, F. Weak topological insulators and composite Weyl semimetals: β-Bi_4X_4. *Phys. Rev. Lett.* **116**, 066801 (2016).
25. Shumiya, N. et al. Evidence of a room-temperature quantum spin Hall edge state in a higher-order topological insulator. *Nat. Mater.* **21**, 1111–1115 (2022).
26. Noguchi, R. et al. Evidence for a higher-order topological insulator in a three-dimensional material built from van der Waals stacking of bismuth-halide chains. *Nat. Mater.* **20**, 473–479 (2021).
27. Yoon, C., Liu, C.-C., Min, H. & Zhang, F. Quasi-one-dimensional higher-order topological insulators. *arXiv preprint arXiv:2005.14710* (2020).
28. Zhou, J.-J., Feng, W., Liu, C.-C., Guan, S. & Yao, Y. Large-gap quantum spin Hall insulator in single layer bismuth monobromide Bi_4Br_4. *Nano Lett.* **14**, 4767–4771 (2014).
29. Zhuang, J. et al. Epitaxial growth of quasi-one-dimensional bismuth-halide chains with atomically sharp topological non-trivial edge states. *ACS Nano* **15**, 14850–14857 (2021).
30. Han, J., Xiao, W. & Yao, Y. Quasi-one-dimensional topological material Bi_4X_4 (*X*=Br, I). *Adv. Phys. X* **7**, 2057234 (2022).
31. Fu, L., Kane, C. L. & Mele, E. J. Topological insulators in three dimensions. *Phys. Rev. Lett.* **98**, 106803 (2007).
32. Qian, X., Liu, J., Fu, L. & Li, J. Quantum spin Hall effect in two-dimensional transition metal dichalcogenides. *Science* **346**, 1344–1347 (2014).
33. Weng, H., Yu, R., Hu, X., Dai, X. & Fang, Z. Quantum anomalous Hall effect and related topological electronic states. *Adv. Phys.* **64**, 227–282 (2015).
34. König, M. et al. Quantum spin Hall insulator state in HgTe quantum wells. *Science* **318**, 766–770 (2007).
35. Huang, J. et al. Room-temperature topological phase transition in quasi-one-dimensional material Bi_4I_4. *Phys. Rev. X* **11**, 031042 (2021).
36. von Schnering, H. G., von Benda, H. & Kalveram, C. Wismutmonojodid BiJ, eine Verbindung mit Bi (O) und Bi (II). *Z. Anorg. Allg. Chem.* **438**, 37–52 (1978).
37. Zhao, W. et al. Topological electronic structure and spin texture of quasi-one-dimensional higher-order topological insulator Bi_4Br_4. *Nat. Commun.* **14**, 8089 (2023).
38. Zhong, J. et al. Towards layer-selective quantum spin hall channels in weak topological insulator $Bi_4Br_2I_2$. *Nat. Commun.* **14**, 4964 (2023).
39. Yang, M. et al. Large-gap quantum spin Hall state and temperature-induced Lifshitz transition in Bi_4Br_4. *ACS Nano* **16**, 3036–3044 (2022).
40. Zhong, J. et al. Facet-dependent electronic quantum diffusion in the high-order topological insulator Bi_4Br_4. *Phys. Rev. Appl.* **17**, 064017 (2022).
41. Noguchi, R. et al. A weak topological insulator state in quasi-one-dimensional bismuth iodide. *Nature* **566**, 518–522 (2019).
42. Autès, G. et al. A novel quasi-one-dimensional topological insulator in bismuth iodide β-Bi_4I_4. *Nat. Mater.* **15**, 154–158 (2016).
43. Xu, R. et al. Development of a laser-based angle-resolved-photoemission spectrometer with sub-micrometer spatial resolution and high-efficiency spin detection. *Rev. Sci. Instrum.* **94**, 023903 (2023).
44. Qi, X.-L. & Zhang, S.-C. Topological insulators and superconductors. *Rev. Mod. Phys.* **83**, 1057–1110 (2011).
45. Wang, Y., Lee, G.-H. & Ali, M. N. Topology and superconductivity on the edge. *Nat. Phys.* **17**, 542–546 (2021).
46. Wu, Y., Liu, H., Liu, J., Jiang, H. & Xie, X. C. Double-frequency Aharonov-Bohm effect and non-Abelian braiding properties of Jackiw-Rebbi zero-mode. *Nat. Sci. Rev.* **7**, 572–578 (2019).
47. Karzig, T. et al. Scalable designs for quasiparticle-poisoning-protected topological quantum computation with Majorana zero modes. *Phys. Rev. B* **95**, 235305 (2017).
48. Schindler, F. et al. Higher-order topology in bismuth. *Nat. Phys.* **14**, 918–924 (2018).
49. Cheng, E. et al. Critical topology and pressure-induced superconductivity in the van der Waals compound $AuTe_2Br$. *npj Quantum Mater.* **7**, 93 (2022).
50. Guo, Z., Deng, J., Xie, Y. & Wang, Z. Quadrupole topological insulators in $Ta_2M_3Te_5$ (M = Ni, Pd) monolayers. *npj Quantum Mater.* **7**, 87 (2022).
51. Wong, K. H. et al. Higher order topological superconductivity in magnet-superconductor hybrid systems. *npj Quantum Mater.* **8**, 31 (2023).
52. Almoalem, A. et al. Charge transfer and spin-valley locking in 4Hb-TaS_2. *npj Quantum Mater.* **9**, 36 (2024).
53. Zhang, J. et al. Observation of dimension-crossover of a tunable 1D Dirac fermion in topological semimetal $NbSi_xTe_2$. *npj Quantum Mater.* **7**, 54 (2022).
54. Filatova, T. G. et al. Electronic structure, galvanomagnetic and magnetic properties of the bismuth subhalides Bi_4I_4 and Bi_4Br_4. *J. Solid State Chem.* **180**, 1103–1109 (2007).
55. Kresse, G. & Furthmüller, J. Efficient iterative schemes for ab-initio total-energy calculations using a plane-wave basis set. *Phys. Rev. B* **54**, 11169–11186 (1996).
56. Heyd, J., Scuseria, G. E. & Ernzerhof, M. Hybrid functionals based on a screened Coulomb potential. *J. Chem. Phys.* **118**, 8207–8215 (2003).
57. Mostofi, A. A. et al. wannier90: a tool for obtaining maximally-localised Wannier functions. *Comput. Phys. Commun.* **178**, 685–699 (2008).
58. Sancho, M. L., Sancho, J. L., Sancho, J. L. & Rubio, J. Highly convergent schemes for the calculation of bulk and surface Green functions. *J. Phys. F* **15**, 851 (1985).

Acknowledgements

This work is funded by the National Natural Science Foundation of China (Grants Nos. 92365204, 12274251, and 62275061) and the National Key R&D Program of China (Grants Nos. 2022YFA1403100 and 2022YFA1403200).

Author contributions

L.X.Y. conceived the experiments. W.X.Z. carried out ARPES measurements with the assistance of X.D., Y.D.L., K.Y.Z., Y.Q.H and Z.K.L. Ab-initio calculations were performed by J.J.Z. Single crystals were synthesized and characterized by M.Y., J.C.Z., and Y.D. The paper was written by W.X.Z.,

L.X.Y., and Y.L.C. All authors contributed to the scientific planning and discussion.

Competing interests
The authors declare no competing interests.

Additional information
Correspondence and requests for materials should be addressed to Y. Du, J. J. Zhou, Y. L. Chen or L. X. Yang.

Reprints and permissions information is available at http://www.nature.com/reprints

Publisher's note Springer Nature remains neutral with regard to jurisdictional claims in published maps and institutional affiliations.